Journal of Power Sources 196 (2011) 1983–1991

Contents lists available at ScienceDirect

Journal of Power Sources

journal homepage: www.elsevier.com/locate/jpowsour

Random-packing model for solid oxide fuel cell electrodes with particle size distributions

Yanxiang Zhang[a], Yunlong Wang[a], Yao Wang[a], Fanglin Chen[b], Changrong Xia[a,b,*]

[a] CAS Key Laboratory of Materials for Energy Conversion, Department of Materials Science and Engineering, University of Science and Technology of China, Hefei, 230026 Anhui, China
[b] Department of Mechanical Engineering, University of South Carolina, Columbia, SC 29208, USA

ARTICLE INFO

Article history:
Received 19 August 2010
Received in revised form
26 September 2010
Accepted 27 September 2010
Available online 7 October 2010

Keywords:
Solid oxide fuel cell
Three-phase boundary
Particle size distribution
Model
Composite electrode

ABSTRACT

A percolation theory based model considering particle size and its distribution is proposed for composite electrodes of solid oxide fuel cells (SOFCs). The model calculation agrees excellently with 3D numerical reconstruction results, suggesting great validity of prediction. Moreover, it is also consistent well with experiment for real LSM (lanthanum strontium manganite)–YSZ (yttria-stabilized zirconia) electrodes with different composition, especially in range from 40:60 to 60:40 wt.% LSM:YSZ. The model can explicitly capture the effects of particle size, distribution, and electrode composition on several basic microstructure features and electrochemical properties of composite electrodes, such as coordination numbers and percolation probability, total and active three-phase boundary length, and interfacial polarization resistance. The model is further used to estimate LSM–YSZ electrode performance with the particle size and distribution of the source materials. The estimation generally coincides with the experiment, showing great potential in predicting power density based on the particle parameters of source materials for SOFCs.

1. Introduction

Solid oxide fuel cell (SOFC) is a potentially important technique of power sources due to its high efficiency [1]. Nonetheless, substantial technical questions remain challenge, such as how to minimize the electrochemical polarization resistance loses at their electrodes, especially the cathodic lose since activating oxygen molecular is more difficulty than hydrogen [2]. A typical cathode is a porous composite consisting of an electro-catalyst phase, which is also an electronic conductor, and an ionic conduction phase [3]. Oxygen reduction at the cathode is a complex process comprising several elementary reactions and transport steps that take place at different sites of the porous composite. Transports of gas-phase oxygen, electron, and oxygen ion are conducted at the electrode pores, electro-catalyst, and ion-conduction phase, respectively. Adsorbing oxygen molecular, splitting the molecular to oxygen species, and diffusing to the charge-transfer site occur at the surface of the electro-catalyst. And finally, the charge-transfer step is considered to occur at sites where the reaction constituents (electrons, ions, and oxygen species) can simultaneously coexist [3]. Lack of any phase, insufficient electro-catalyst surface area or inadequate site for charge-transfer will ultimately lessen the overall oxygen reduction rate, i.e. increase the polarization lose.

Therefore, the electrode properties such as interfacial polarization resistance are microstructure dependence. The electrode microstructure is frequently illustrated as a random packing system of sphere particles as shown in Fig. 1a. The key microstructure parameter affecting the electrochemical response is the sites for charge-transfer reaction, often termed as three-phase boundaries (TPB), where ionic particle, electronic particle, and pore contact (Fig. 1b). A volume of work shows that for many SOFC electrodes, overall performance scales with TPB length [4,5]. It should be noted that an active TPB is not only a site where the three phases meet as shown in Fig. 1b, but also a site to which the three distinct reactants (electrons, oxygen ions, and oxygen species) are transported and coexist. While almost all of pores are available for gas transportation [6], not every ionic/electronic particle is available for ion/electron conduction due to stochastic-packing nature of particles. That is, only part of the three-phase meeting sites are electrochemical active. Those TPBs are active when their ionic and electronic particles belong to percolating ionic and electronic clusters, respectively. Fig. 1c shows a percolated cluster. The other TPBs such as the insulated clusters shown in Fig. 1d, which are formed with particles not connected to the percolated ionic/electronic phases, are not active since either electrons or oxygen ions are not available at these sites. Consequently, active TPB length is smaller than the total value and is also structure sensitive.

* Corresponding author at: Department of Materials Science and Engineering, University of Science and Technology of China, Hefei, 230026 Anhui, China.
Tel.: +86 551 3607475; fax: +86 551 3601592.
E-mail address: xiacr@ustc.edu.cn (C. Xia).

0378-7753/$ – see front matter © 2010 Elsevier B.V. All rights reserved.
doi:10.1016/j.jpowsour.2010.09.098

Nomenclature

f	probability density (μm^{-1})
L	length per unit volume (μm^{-2})
Log N	lognormal distribution
M	sampling object which can be particle number or volume
N	normal distribution
P	percolation probability
R	resistance ($\Omega\,cm^2$)
r	particle radius (μm)
S	surface-area fraction
U	uniform distribution
Z	coordination number

Greek letters

ϕ	volume fraction
σ	standard deviation of particle distribution (μm)
μ	mean particle radius (μm)
θ	contact angle
ρ	resistivity ($\Omega\,cm$)
δ	electrode thickness (μm)
λ	effective thickness of electrode (μm)

Subscripts

i	ionic particles
j	electronic particles
g	pores
p	polarization
TPB	three-phase boundary
-	particles have a distribution

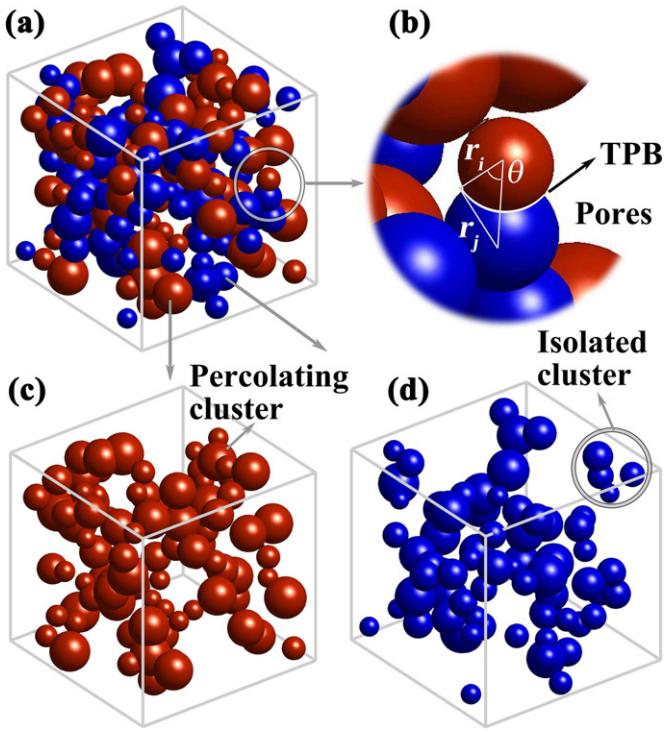

Fig. 1. Schematic diagrams of a random parking system. (a) A porous two-phase composite electrode with particle size distributions, (b) three-phase boundary, (c) the network of ionic particles, and (d) the electronic particles showing an isolated cluster that does not contribute to active TPB.

Theoretically, the active TPB length can be quantitatively related to the two-phase particle sizes and porosity [7–9]. However, earlier models assume that particles are mono-sized, rather than the case with a size distribution in question. Thus, those simulations do not capture the effects of particle distributions on electrode performance. Recently, Gokhale et al. [10] proposed a stochastic geometry based model (SGM), relating total (active + inactive) TPB length to mean size and standard deviation of particles. They have shown that mono-sized particles lead to high total TPB length compared to the particles having size distributions. However, particle size distributions have more complex effects on TPB length according to the numerical reconstruction of composite electrodes [6]. In addition, particle size distribution itself is much more complicated than a uniform distribution with standard deviation. Thus, it is of interest to develop accurate relationships between particle size distributions and electrode properties such as active TPB length and interfacial polarization resistance.

In this work, we propose an approach based on percolation theory and particle-layer model [9] to explicitly capture the effects of particle size distributions on total and active TPB lengths and interfacial polarization resistance. Although the method and results presented here are general and can be applied to both composite anodes and cathodes, for this work, we have denoted the electrocatalyst phase, which is also an electronic conduction phase, as lanthanum strontium manganite (LSM) and the oxygen-ion conducting phase as yttria-stabilized zirconia (YSZ) to represent a composite cathode and further to validate our model.

The present model shows that TPB length and electrochemical performance are very sensitive to particle sizes and their distributions. However, these parameters are seldom practically known due to the difficulty in phase identification. A combination of focused ion beam (FIB) [11,12], Auger electron spectroscopy elemental mapping, and secondary electron imaging has been successfully used for imaging the YSZ and LSM phases [13]. Recently, another combination of chemical etching technique and atomic force microscopy is developed to observe these phases [14]. Nevertheless, revealing the size and its distribution is very time consuming and relays on equipments that are not readily available in most research laboratories. Here, an estimation method is proposed to determine the particle size and distribution from the source materials.

The LSM–YSZ porous cathode, which is used as the example electrode in this work, is usually processed with LSM and YSZ powders, typically by coating a mixture consisting of the LSM and YSZ particles onto a dense YSZ electrolyte substrate using a slurry-based technique such as screen-printing, followed by co-sintering the two-phase particles. The LSM and YSZ particles are fabricated with various techniques such as solid-state reaction, co-precipitation, and combustion. Whatever, the last step is via firing to form perovskite structured LSM and fluorite structured YSZ. The firing temperature is usually close to the co-sintering temperature, which is used to form the composite cathode. So, particle growth in the co-sintering process is negligible when the firing temperature is close to or higher than the co-sintering temperature. In addition, in a porous composite system consisting of two phases which do not react with each other, particle growth (grain growth) of one phase is limited by the other phase. For example, compared with pure LSM phase, LSM particle growth in a LSM–YSZ composite is much less significant even after it is sintered at 1200 °C [15]. Consequently, in most cases when the sintering temperature is not too high, the particle size in the cathode is equal or closes to that of the initial powder. Thus, particle size and distribution of the initial powder roughly represent the size and distribution of the particle in a sintered electrode.

Accordingly, the electrochemical performance could be predicted with our model regarding the particle size and its

distribution of the initial LSM and YSZ powders. So, in this work, in addition to general model development, interfacial polarization resistances of LSM–YSZ cathodes, which are prepared with different YSZ particles, are theoretically predicted and experimentally determined. The theoretical prediction generally agrees with the experimental results, suggesting that it is possible to predict the electrode performance with the original powder properties such as particle size and distribution. Since the electrolyte conductivity is well known, this work points out a path through which power density of SOFCs (at least single cells) could be predicted from the characteristics of raw powders. This is a new approach which is here named as a from-powder-to-power path.

2. Theoretical development

Actual structures of composite electrodes are different from the random packing systems, but this approach has been proven to be successful in correlating micro-structure parameters and electrochemical performance of composite electrodes [2,8]. Properties of random packing system of binary spherical particles can be estimated using percolation theory. The concept of coordination number is central for the implementation of percolation theory. For example, in a binary mixture of *i* type (the ionic conduction phase) and *j* type (the electronic conduction phase) particles with radiuses of r_i and r_j, respectively, the coordination number, $Z_{i,j}$, between an *i* type particle and all *j* type particles holds [16],

$$Z_{i,j} = \frac{\overline{Z}}{2}\left(1 + \frac{r_i^2}{r_j^2}\right) S_j \tag{1a}$$

where $\overline{Z}$ indicates the overall average coordination number of the two-phase system and the value is typically 6; S_j is the surface-area fraction of *j* type particles relative to all particles,

$$S_j = \frac{\phi_j/r_j}{\phi_i/r_i + \phi_j/r_j} \tag{1b}$$

where ϕ_i is the volume fraction of phase *i* relative to all solid phases.

To illustrate the effects of particle distributions, uniform (*U*), normal (*N*), and lognormal (Log*N*) distributions are considered. Fig. 2 shows the definition of these distributions with the same mean particle radius, μ, and standard deviation, σ. The probability density, *f*, is defined as,

$$f(r) = \begin{cases} \dfrac{1}{2\sigma}, & \text{for } r \in [\mu-\sigma, \mu+\sigma] \\ 0, & \text{otherwise} \end{cases} \tag{2a}$$

for the uniform distribution $U(\mu,\sigma)$ (Fig. 2a);

$$f(r) = \frac{1}{\sigma\sqrt{2\pi}A}\exp\left(\frac{-(r-\mu)^2}{2\sigma^2}\right), \quad \text{for } r > 0 \tag{2b}$$

for the normal distribution $N(\mu,\sigma)$ (Fig. 2b), where *A* is normalization constant making up for the restriction of $r > 0$; and

$$f(r) = \frac{1}{rn\sqrt{2\pi}}\exp\left(\frac{-(\ln r - m)^2}{2n^2}\right), \quad \text{for } r > 0 \tag{2c}$$

for the lognormal distribution $\mathrm{Log}N(\mu,\sigma)$ (Fig. 2c), where $m = \ln(\mu^2/\sqrt{\sigma^2+\mu^2})$ and $n = \sqrt{\ln(\sigma^2/\mu^2+1)}$.

However, any type of distribution can be implemented, such as a real case shown in Fig. 2d [17]. In practical, SOFC powders always permit the successful application of lognormal distribution [17–19]. As shown in Fig. 2a, the differential element, $f(r)dr$, indicates the fraction of particles with radius between *r* and $r+dr$. It should be noticed that the physical meaning of the fraction can be volume fraction or number fraction, represented as the subscript $M = V$ or *N*, respectively. This depends on sampling object.

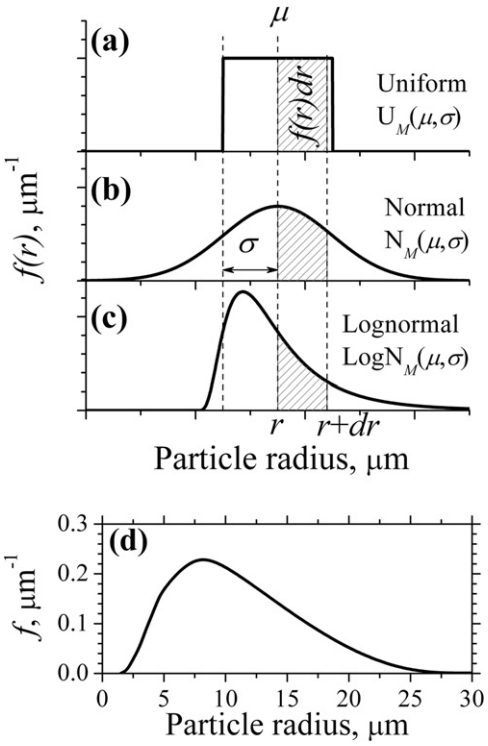

Fig. 2. Definition of particle size distributions. (a) Uniform, (b) normal, (c) lognormal, and (d) an actual distribution of YSZ particles [17].

For instance, the sampling object of a laser particle size analyzer is particle volume [17], while the method in Ref. [6] and this study uses particle number as the sampling object.

Considering *j* type particles are poly-dispersed with *i* type particles mono-sized, the surface-area fraction of *j* type particles with radius between r_j and $r_j + dr_j$ relative to all particles is,

$$dS_j = \frac{\phi_j f_j dr_j/r_j}{\phi_i/r_i + \phi_j\left\langle 1/r_j\right\rangle} \tag{3a}$$

where $\langle 1/r_j\rangle$ indicates mean value of $1/r_j$, defined as $\left\langle 1/r_j\right\rangle = \int f_j/r_j dr_j$. The probability density function, *f*, is with respect to volume fraction of particles. That is to say the sampling object is particle volume. In principle, the probability density function regarding particle number can be derived from *f* as Bf/r^3, where parameter *B* denotes normalization constant. Clearly, the coordination number between an *i* type particle and *j* type particles with radius between r_j and $r_j + dr_j$ can be estimated as

$$dZ_{i,\underline{j}} = \frac{\overline{Z}}{2}\left(1 + \frac{r_i^2}{r_j^2}\right) dS_j \tag{3b}$$

where underline "_" represents particles have a distribution.

Combining with Eqs. (3a) and (3b), the coordination number between an *i* type particle and all *j* type particles is,

$$Z_{i,\underline{j}} = \int dZ_{i,\underline{j}} = \frac{\overline{Z}}{2}\frac{\phi_j}{\phi_i/r_i + \phi_j\left\langle 1/r_j\right\rangle}\int\left(1 + \frac{r_i^2}{r_j^2}\right)\frac{f_j}{r_j}dr_j \tag{4a}$$

Considering *i* type particles also have a size distribution f_i, the average coordination number between an *i* type particle and all *j* type particles is given by,

$$Z_{\underline{i},\underline{j}} = \int Z_{i,\underline{j}} dN_i \tag{4b}$$

where dN_i indicates the particle number fraction of i type particles with radius between r_i and $r_i + dr_i$ relative to total i type particle numbers,

$$dN_i = \frac{f_i dr_i / r_i^3}{\langle 1/r_i^3 \rangle} \tag{4c}$$

Combining with Eqs. (4a)–(4c), the average coordination number is obtained for the two-phase particles with size distributions,

$$Z_{\underline{i,j}} = \frac{\overline{Z}}{2} \frac{1}{\langle 1/r_i{}^3 \rangle} \frac{\phi_j}{\phi_i \langle 1/r_i \rangle + \phi_j \langle 1/r_j \rangle} \iint \left(\frac{1}{r_i{}^3 r_j} + \frac{1}{r_i r_j{}^3} \right) f_i f_j dr_i dr_j \tag{5}$$

The coordination number between i type particles, $Z_{\underline{i,i}}$, and j type particles, $Z_{\underline{j,j}}$, can be obtained by simply substituting the subscripts j and i in Eq. (5), respectively.

Similar to binary system with mono-sized particles [7], the probability of an i type particle belonging to the percolating cluster is estimated as,

$$P_i = \left[1 - \left(\frac{4.236 - Z_{\underline{i,i}}}{2.472} \right)^{2.5} \right]^{0.4} \tag{6}$$

Consequently, active TPB length per unit volume can be expressed as,

$$L_{\mathrm{TPB}} = P_i P_j \int 2\pi \sin\theta \min(r_i, r_j) Z_{\underline{i,j}} \frac{(1-\phi_g)\phi_i f_i}{4\pi r_i^3/3} dr_i \tag{7}$$

In Eq. (7), the integral item indicates total TPB length per unit volume; $((1-\phi_g)\phi_i f_i / 4\pi r_i^3/3) dr_i$ is the number of i type particles with radius between r_i and $r_i + dr_i$ per unit volume, where ϕ_g is electrode porosity; θ indicates the contact angle between a smaller particle and a bigger particle as illustrated in Fig. 1b. The value of θ is usually assumed between 15° and 90° [8,20], which is sensitive to experimental condition. Combining Eqs. (4a) and (7) gives the following expression for active TPB length per unit volume:

$$L_{\mathrm{TPB}} = \frac{3}{4} \sin\theta \overline{Z} P_i P_j \frac{(1-\phi_g)\phi_i \phi_j}{\phi_i \langle 1/r_i \rangle + \phi_j \langle 1/r_j \rangle} \iint \min(r_i, r_j) \times \left(\frac{1}{r_i{}^3 r_j} + \frac{1}{r_i r_j{}^3} \right) f_i f_j dr_i dr_j \tag{8}$$

It should be noticed that when standard deviation of particles tends to be zero, that is the particles tend to be mono-sized, Eq. (8) can degrade into the formula based on the classical percolation theory [9].

Combining with the particle-layer model, interfacial polarization resistance can be estimated as [9],

$$R_p = \rho_i \lambda \coth\left(\frac{\delta}{\lambda} \right) \tag{9a}$$

where δ indicates electrode thickness; ρ_i is resistivity of ionic phase,

$$\rho_i = \rho_i^0 [(1-\phi_g)\phi_i P_i]^{-\gamma} \tag{9b}$$

in which ρ_i^0 is the intrinsic resistivity, and γ is the Bruggeman factor that accounts for tortuous ion-conduction pathways and the value is typically 1.5; λ is the effective electrode thickness within which electrochemical reactions mainly take place and is estimated as,

$$\lambda = \sqrt{\frac{\rho_{\mathrm{TPB}}}{\rho_i L_{\mathrm{TPB}}}} \tag{9c}$$

where ρ_{TPB} is the resistivity of TPB derived from electrochemical reactions.

3. Experimental procedure

LSM–YSZ composite cathodes were prepared onto YSZ electrolytes using screen-printing, a typical electrode processing technique. To prepare the YSZ electrolyte substrates, 8 mol% Y_2O_3 stabilized zirconia (YSZ) powder (Jiujiang Fanmeiya Advanced Materials Co., Ltd., China) was cold-pressed under 20 MPa to form green pellets. The samples were then sintered at 1350 °C for 5 h, resulting in dense YSZ substrates with the diameter of about 10 mm and the thickness of 0.5 mm. LSM powder was synthesized using a glycine-nitrate method [21] and fired at 900 °C to form the perovskite structure. Commercial YSZ powders with different particle sizes were cooperated with LSM to form the composite cathodes. The relative coarse YSZ powder with big particle size is represented with C-YSZ, the fine one with small size is called as F-YSZ, and the medium one is named as M-YSZ. To determine the particle size and its distributions, the LSM and YSZ powders were ultrasonically dispersed for 5 min and observed with scanning electron microscope (SEM, JSM-6700F, JEOL). The particle size was measured on the SEM images using Matlab® software. For each sample, 300–400 particles were measured to ensure statistical accuracy. The results are shown in Fig. 3. These sizes can be well fitted to lognormal distribution. The mean particle radius and standard deviation are also shown. To fabricate composite cathodes, LSM powder was mixed with F-YSZ, M-YSZ and C-YSZ powders, respectively, and then milled with ethyl cellulose to form uniform slurries. Symmetrical half-cells were prepared by coating the slurry on both surfaces of the YSZ electrolytes using the screen-printing technique. The cathodes were then co-fired with the electrolytes at 1000 °C for 2 h to produce a ~50 μm-thick electrode layer. Two parallel-samples were fabricated for each combination. Pt paste and Ag wires were used for current collection. An electrochemical station (IM6e, ZAHNER) was used to evaluate the interfacial polarization resistance. The measurement was conducted under open-circuit conditions with an amplitude 10 mV in the frequency range 0.01 Hz–1 MHz.

4. Results and discussion

4.1. Coordination number

Coordination number is the core parameter of the percolation theory. It is therefore discussed in this section as a function of particle size distributions including distribution types and sampling objects. To clearly present the distribution effect of one phase, the other phase is assumed to be monosized. Let's start with a case that j type particles are not monosized but satisfy uniform, normal and lognormal distributions with mean particle radius of 0.5 μm and standard deviation of σ_j. Their sampling objects can be particle volume and particle number. The electrode has a typical composition of $\phi_i = \phi_j = 0.5$. And the i type particle radius has a monosize of 0.5 μm. Fig. 4 shows the effects of the standard deviation, σ_j, on coordination numbers between ionic–ionic, $Z_{i,i}$ (Fig. 4a), electronic–ionic, $Z_{i,j}$ (Fig. 4b), and electronic–electronic particles, $Z_{j,j}$ (Fig. 4c). When $\sigma_j = 0$, that is j type particles are also mono-sized and the radius is equal to the other's, the calculated coordination numbers are all 3 (Fig. 4). This is in great accordance with earlier models for composites consisting of mono-dispersed particles [9,16].

When the sampling object is given, the trends of coordination numbers are the same for the uniform, normal, and lognormal distributions. For instance, when σ increases, which means a broader distribution, and the object is particle number, $Z_{j,j}$ and $Z_{i,j}$ decrease while $Z_{i,i}$ increases. Increasing σ_j for the number objected distribution means the distribution is broadened almost equally (exactly

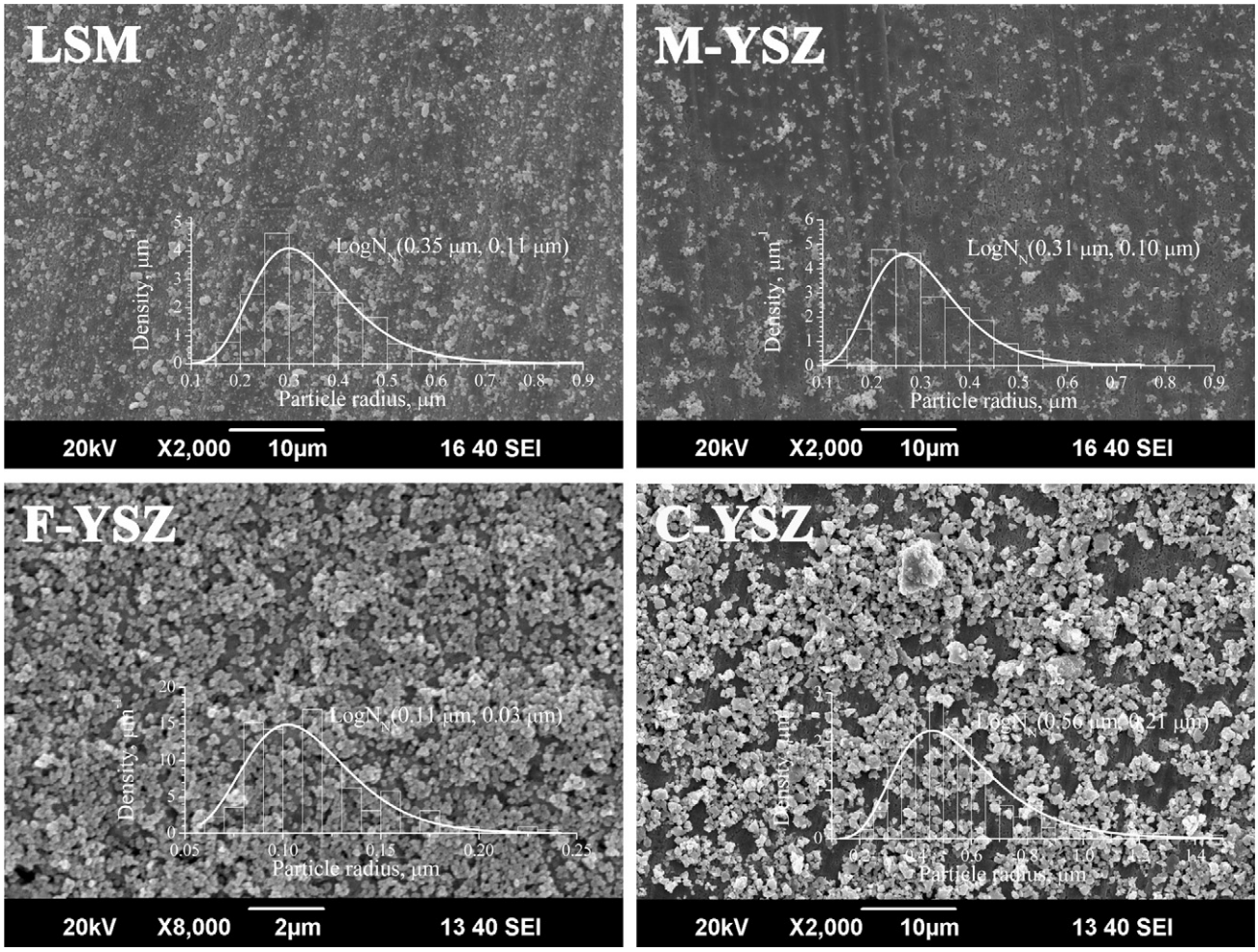

Fig. 3. SEM graphs showing the particles and distributions for LSM, F-YSZ, M-YSZ, and C-YSZ powders.

equal for uniform and normal distribution) by the number of small and big particles. However, the big particles occupy more space. Thus, increasing σ_j is equivalent to increasing j type particle size. That is to say, the larger particles act a more important role in the whole particle range when particle number is of concern. On the contrary, the numbers exhibit opposite trend when the object is volume. In this case, increasing σ causes extraordinary enlarging in small particle number. So, decreasing the coordination number between i particles, $Z_{i,i}$, in accompanied by increasing the coordination number related to j particles, i.e. $Z_{j,j}$ and $Z_{i,j}$. Increasing in $Z_{i,i}$ and $Z_{j,j}$ indicates high percolation probability for i and j phase, consequently, the enhancement of ion and electron conducting ability, respectively. Unfortunately, as shown in Fig. 4a and c, increasing coordination number of one phase results in the decrease of the other. Practically, $Z_{i,i}$ should have a high value since the oxygen-ion conductivity is much lower than the electronic one. High $Z_{i,j}$ value indicates high TPB length, therefore improving electrochemical performance.

Fig. 4 also shows that, although the curvilinear trend is the same for the distributions termed with uniform, normal, and lognormal, absolute change in coordination number is quite difference. While the changes are comparable for the normal and lognormal distributions, the change for the uniform distribution is much less significant even though σ is the same. This is because the ranges of the normal and lognormal distributions are comparable and they are much wider than that of the uniform distribution, as shown in Fig. 2.

4.2. Percolation probability

Fig. 5 shows the percolation probability, P_j, as a function of volume fraction, ϕ_j, when j particles have distributions with mean radius of 0.5 μm and standard deviation of 0.2 μm and i particles are monosized, $r_i = 0.5$ μm. When both phases have the same size, i.e. $r_j = 0.5$ μm as shown in Fig. 5, the same curve can be also calculated using our previous model for composites composed of monosized particles [9]. Compared with the mono-sized case, when the sampling object is particle number, percolation probability decreases and volume fraction threshold shifts to a high level. The prediction suggests more j type phase should be used to maintain the same percolation probability. This is in accordance with the results derived from 3D numerical simulation [6]. On the other hand, when the sampling object is particle volume, percolation probability increases, and volume fraction threshold tends to be low. The tendency is much more significant for the normal and lognormal distributions because of the wider range compared with the uniform distribution.

4.3. Active TPB length

Fig. 6 shows how the particle size distribution can affect active TPB length at various electrode compositions. Normal distribution is implemented to compare with the 3D numerical reconstruction results [6] and SGM approach [10]. The contact angle θ is assumed as 34.4° according to the cross-section of 3D reconstructed electrode.

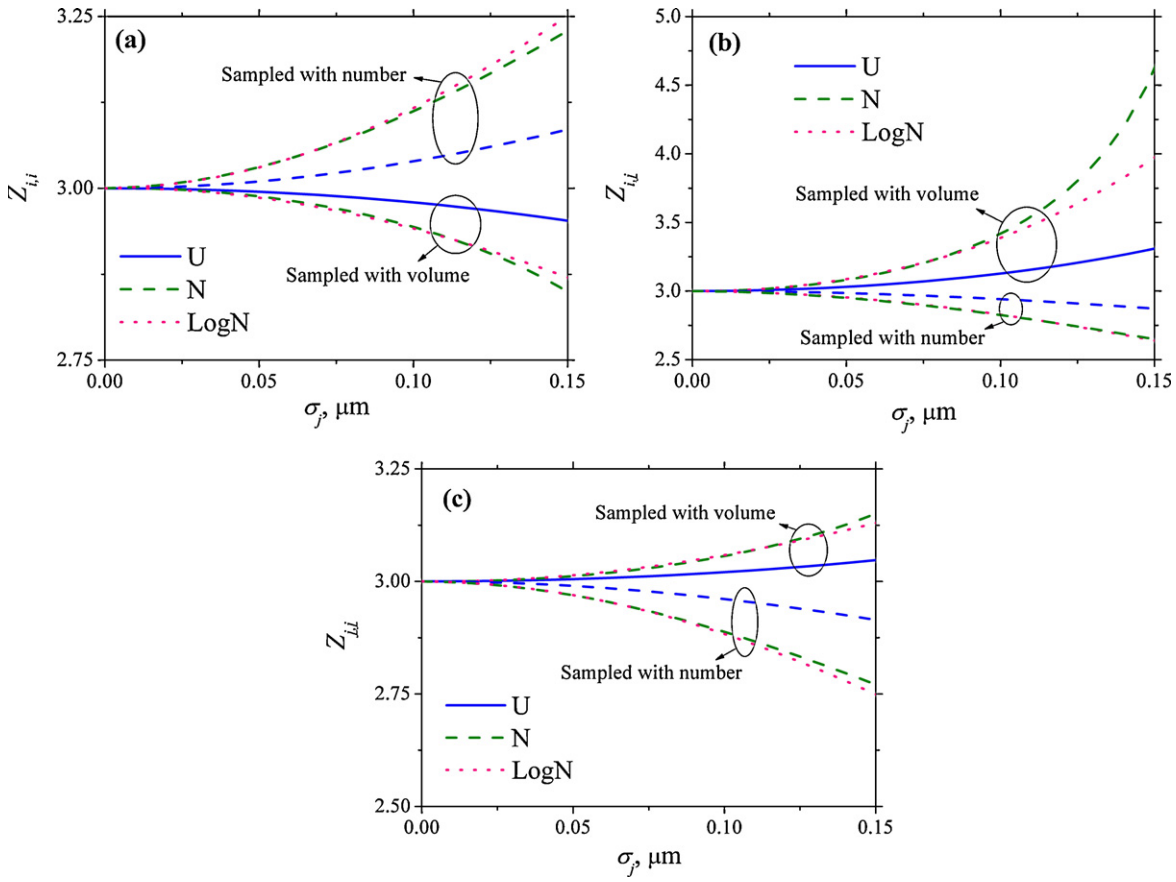

Fig. 4. Effects of standard deviation, σ_j, on coordination numbers for j type particles with uniform (U), normal (N), and lognormal (Log N) distributions ($\phi_i = \phi_j = 0.5$, $r_i = 0.5$ μm, $\mu_j = 0.5$ μm). (a) Coordination number within i type particles, (b) between i type and j type particles, and (c) within j type particles.

Fig. 6a shows the comparison of active TPB length derived from 3D reconstruction, SGM model, and the present approach. When the sampling object is number, all the three results show that the active TPB length derived with particle distributions of $r_i = r_j = N_N$ (0.25 μm, 0.1 μm) is lower than that with monosized particles, $r_i = r_j = 0.25$ μm. This phenomenon is mainly caused by the decrease of coordination number $Z_{i,j}$ (Fig. 4b) and percolation probability (Fig. 5) when the particles have a distribution termed with number. These methods also demonstrate that the highest TPB length is observed at $\phi_i = \phi_j$ when the two phases have the same particle sizes and distributions. However, there are differences in the results derived by the three methods. Our model calculation agrees well with the 3D reconstruction result in the whole composition range limited by the percolation requirement. Compared with the 3D reconstruction method, the model can be easily conducted because it is analytic. Indeed, by given specific knowledge for particular electrode micro-structures, the model can be applied to predict general results and explicitly capture the dependence of active TPB length on particle size distribution. Fig. 6a also shows that our model produces better agreement with 3D reconstruction data than SGM model in a wider composition range. To the best of our knowledge, SGM approach is the only available model considering particle size distributions on TPB length calculation. Nonetheless, SGM calculates total TPB length including effective and non-effective sites. As shown in Fig. 1, not all the TPBs are active for electrochemical reaction since some sites are only physical interfaces where the ion-conduction phase, electro-catalyst phase, and pore meet, not those sites for charge-transfer reaction where oxygen ions, electrons, and oxygen molecular coexist. It should be noted that at typical composition range $\phi_j = 0.4$–0.6, about 90% of total TPBs is active as shown in Fig. 5. Furthermore, SGM concludes that the maximum TPB length always corresponds to the composition of $\phi_i = \phi_j = 0.5$ disregarding difference of particle size distribution. It seems correct as suggested by Fig. 6a. However, the 3D reconstruction and our model show that the composition corresponding to the maximum TPB length is a function of particle size and its distribution, which is discussed in the following sections.

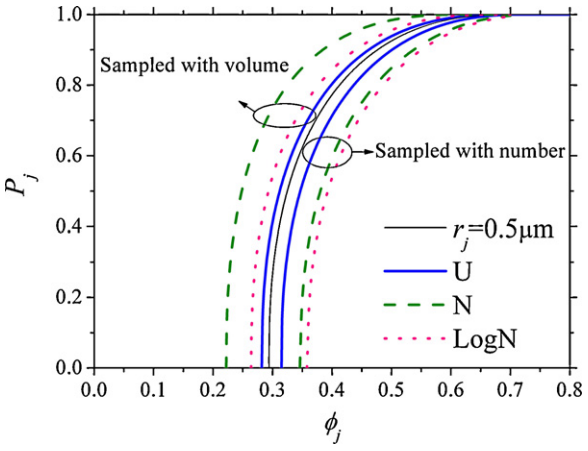

Fig. 5. Effects of j phase volume fraction, ϕ_j, on its percolation probability for various j type particle distributions with $\mu_j = 0.5$ μm and $\sigma_j = 0.2$ μm. The i type phase is monosized, $r_i = 0.5$ μm.

It is of interest to note that if the particle radiuses of both ionic and electronic phases are the same, and they have the same distributions, the volume fraction of ionic or electronic phase corresponding to the maximum active TPB length will be 0.5. How-

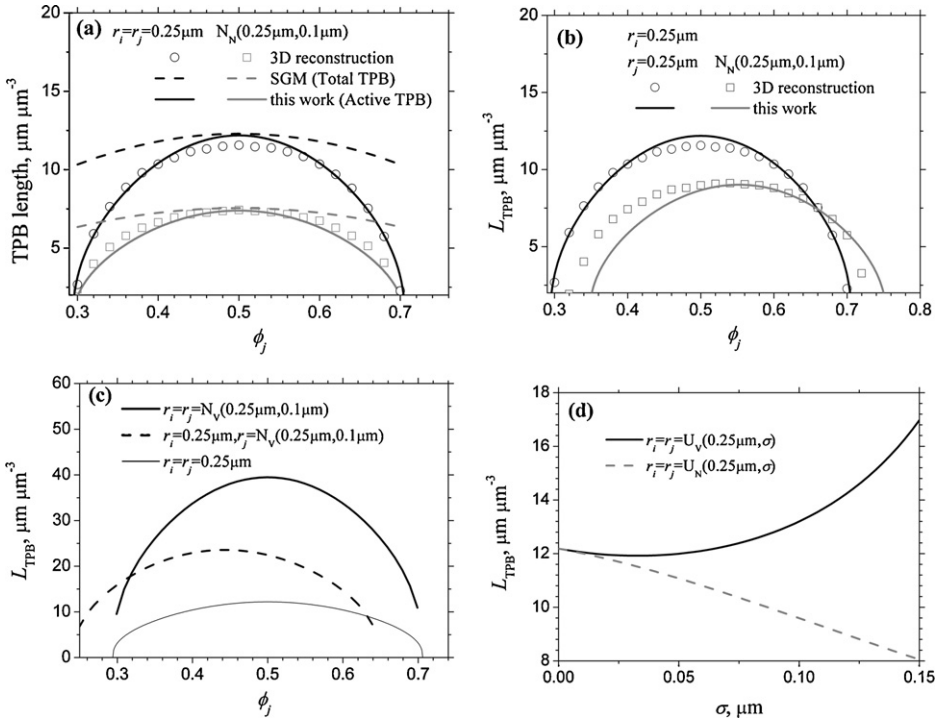

Fig. 6. TPB length for composite electrodes consisting of various particles. Calculation is conducted based on $\phi_g = 0.3$ and $\theta = 34.4^\circ$ according to 3D reconstruction results. (a) Total and active; (b) active TPB length derived by 3D reconstruction [6], SGM model (total TPB length) [10], and the present approach for composite electrodes composed of monosized particles ($r_j = r_i = 0.25\,\mu m$) and of particles with normal size distribution, N_N (0.25 μm, 0.1 μm). The sampling object is particle number; (c) active TPB length derived from different distributions sampled with particle volume; and (d) effects of standard deviation and sampling objects on active TPB length.

ever, the volume fraction can be different when the mean particle radiuses of both phases are same and particle size distributions are different. For instance, in case of $r_i = 0.25\,\mu m$ and $r_j = N_N$ (0.25 μm, 0.1 μm), Fig. 6b demonstrates that ϕ_j corresponding to the maximum active TPB length shifts to 0.55 from 0.5 for $r_i = r_j = 0.25\,\mu m$. This is caused by the increase of ϕ_j threshold as shown in Fig. 5 and the decrease of ϕ_i threshold.

When sampling method is particle volume, the results are different. For instance, as shown in Fig. 6c, in the case of $r_i = 0.25\,\mu m$ and $r_j = N_V$ (0.25 μm, 0.1 μm), the volume fraction, ϕ_j, relating to the maximum TPB length shifts to 0.44, being contrary to that shown in Fig. 6b. Reasons are the increase of P_j (Fig. 5) and the decrease of P_i when the sampling method changes from particle number to volume. On the other hand, in the case of $r_i = r_j = N_V$ (0.25 μm, 0.1 μm), Fig. 6c shows that the active TPB length is remarkably enhanced compared with the mono-sized case, which is also different with the results shown in Fig. 6a. This is the result of $Z_{i,j}$ increase (Fig. 4b). Combining Fig. 6c with Fig. 6a, it can be concluded that when *i* and *j* type particles have the same distribution with respect to particle volume/number, the active TPB length can increase/decrease comparing to its mean size case. This is further confirmed in Fig. 6d. However, it should be noted that when σ is small, there is no obvious difference between the two types of particle size distributions, and smaller number of total particles is required to fill the electrode domain by comparing with large poly-dispersed case. Therefore, active TPB length is reduced.

4.4. Application to a real electrode system

In a real electrode system, particle size and distribution are rarely the same for the two phases. Thus it is of great interest to apply our approach to a real system rather than the 3D numerical reconstruction. But data is seldom reported on the structural details of composite electrodes. Recently, Barnett et al. report the microstructural features of LSM–YSZ electrodes with compositions ranging from 30:70 to 70:30 wt.% LSM:YSZ, including total and active TPB length, which are determined using FIB–SEM technique [12]. The electrodes are prepared with the screen-printing method and sintered at 1175 °C for 1 h. Before printing, LSM and YSZ powders are mixed through ball-milling. Data is not directly available on the particle size distribution for the LSM and YSZ particles in the electrodes. However, using the intercept method [22], it can be estimated from the dispersed particles on the segmented 2D images, which are shown in Fig. 3 of Ref. [12]. Fig. 7a shows the results for particle radius and its distribution. Clearly, LSM and YSZ particles are not of the same size. They can be represented with log-normal distributions, Log N_N (0.27 μm, 0.08 μm) for LSM and Log N_N (0.19 μm, 0.05 μm) for YSZ. The total and active TPB length could be calculated using the present approach. According to the suggestion of Ref. [23], contact angle θ is assumed as 19.5° for the LSM–YSZ systems. Fig. 7b shows the comparison between the prediction and the experimental results obtained with FIB–SEM by Barnett et al. The TPB length is also calculated with SGM model, which deals only with the total length. Our calculation results agree well with experimental data in both the active and the total TPB lengths.

However, it should be noticed that the present model predicts zero active TPB length beyond the composition threshold. As model calculation shown in Fig. 7c, when YSZ composition is beyond the threshold ($\phi_{YSZ} > 0.61$), LSM particles cannot form a percolating cluster, represented by zero percolation probability. Thus there is no active TPB theoretically exists within the electrode, even almost all YSZ particles are percolated. But there exists a small amount of active TPBs according to the FIB–SEM results. These TPBs are mainly close to the current collecting layer. They can be formed by the isolated LSM clusters (Fig. 1d) contacting with the current collector and the percolating YSZ particles. The isolated clusters are not theoretically considered as the active sites in the percolation theory. In addition, the finite domain size used for FIB–SEM may be too small, throughout which the probability of LSM particles

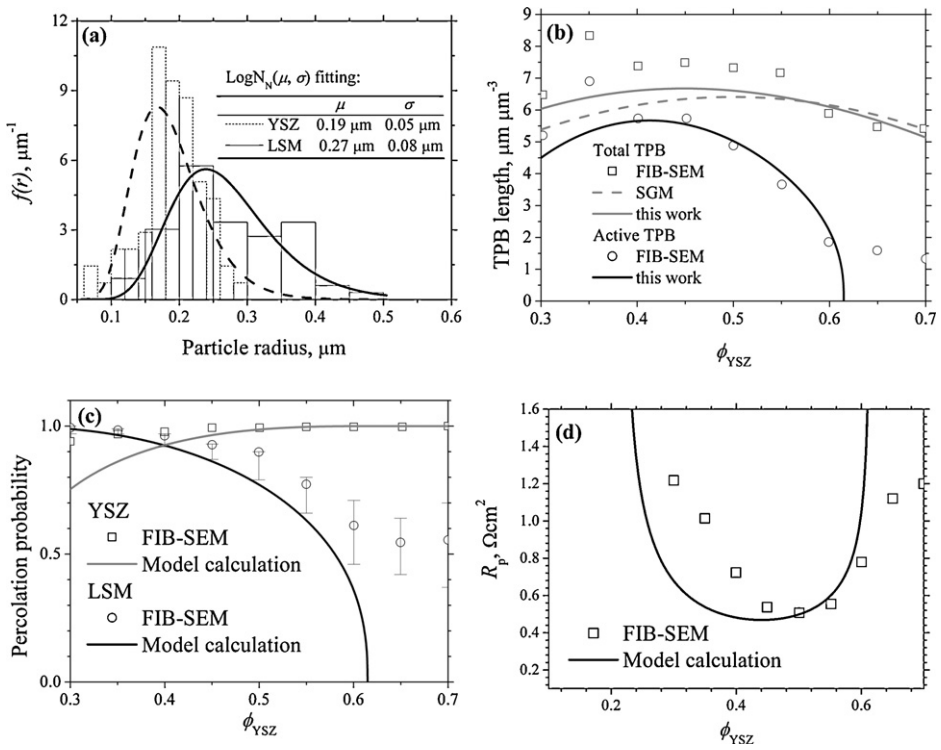

Fig. 7. Comparison between model prediction and experimental results for LSM–YSZ electrodes [12]. (a) Particle size distribution of LSM and YSZ particles derived from Fig. 3 of Ref. [12]; (b) TPB length determined with present approach, SGM model and FIB–SEM method; (c) percolation probabilities; and (d) interfacial polarization resistance ($\phi_g = 0.5$).

can be overestimated. Nevertheless, this difference suggests that those isolated particles and clusters, which are close to the current-collector/cathode interface or electrolyte/cathode interface, should be active for electron or oxygen-ion conduction and thus have to be considered in the future work.

Fig. 7d shows the comparison of interfacial polarization resistances obtained with model prediction and experimental measurements. The resistivities of YSZ and TPB are derived from Ref. [9]. Near the composition of $\phi_{YSZ} = 0.5$, the prediction seems to be in good agreement with the experimental data. For the electrode with porosity of 0.5 and thickness of 11 μm [12], the predicted interfacial resistance is 0.50 Ω cm^2 at 800 °C, being comparable with the reported 0.51 Ω cm^2 for $\phi_{YSZ} = 0.5$. When $\phi_{YSZ} > 0.6$ or $\phi_{YSZ} < 0.4$, the predicted resistance is not consistence with the experimental data. When LSM content is low ($\phi_{YSZ} > 0.6$), the predicted resistance is higher than the measured one. At this composition, almost all the YSZ particles belong to a huge percolated YSZ cluster filling all the electrode space, while almost all the LSM particles are not percolated but form some isolated clusters. TPB formed with the isolated clusters are possibly electrochemical active when the clusters are on the current collector side. For these TPBs, oxygen ions are readily available through the percolated YSZ phase and electrons are also available through the isolated clusters, which connect to the current collector. This underestimates the electrochemical activity when LSM content is low. On the other hand, when YSZ content is lower ($\phi_{YSZ} < 0.4$), the predicted resistance is lower than the measured data. In this case, electrons are readily available throughout the whole cathode since LSM percolation probability is close to 100%. Fortunately, YSZ particles are also percolated and the percolation probability is very high in the experimental composition range due to the relatively small particles (Fig. 7a and c). So, TPB formed with percolated YSZ particles dominates the electrochemical activity although TPB created with isolated YSZ clusters, which connect to the electrolyte layer, contributes also to the activity. The resistance is calculated by combining the active TPB length with particle-layer model [9], in which Bruggeman factor is assumed to be a constant. The factor is a function of the tortuosity of ion-conduction paths, increasing with the decrease of percolation probability. Experimental results also show that the tortuosity of percolated YSZ increased rapidly with the decrease of YSZ content [12]. The increased tortuosity infers the enlarged distance for oxygen ion transportation, leading to the discrepancy between the model prediction and the experimental data. Although discrepancies exist when the volume fractions are quite different for the two phases, the model is useful in predicting electrochemical performance of practical electrodes since in these systems the two phase contents are quite close to achieve high electrode activities.

4.5. TPB length and interfacial polarization resistance estimated with powder sizes

Since FIB–SEM instruments are not readily available for normal laboratories, it is worthy to use the particle size of the source powders to predict TPB length as well as interfacial polarization resistance (area specific resistance), especially when the electrodes are formed at relatively low sintering temperatures. YSZ powders of different size are chosen for such evaluation due to the fact that it is often much harder to sinter YSZ than LSM, particularly at the same sintering temperature. Fig. 8 shows the estimated active TPB length for F-YSZ–LSM, M-YSZ–LSM and C-YSZ–LSM electrodes. The powder particle distributions are fitted using lognormal distribution as shown in Fig. 2. The sampling object is particle number. And the contact angle is assumed as 19.5°. Generally, TPB length decreases when YSZ size increases. The YSZ volume fraction corresponding to the maximal active TPB length is small for fine YSZ. This is caused mainly by the smaller particles with smaller standard deviation of F-YSZ than that of LSM (Fig. 2).

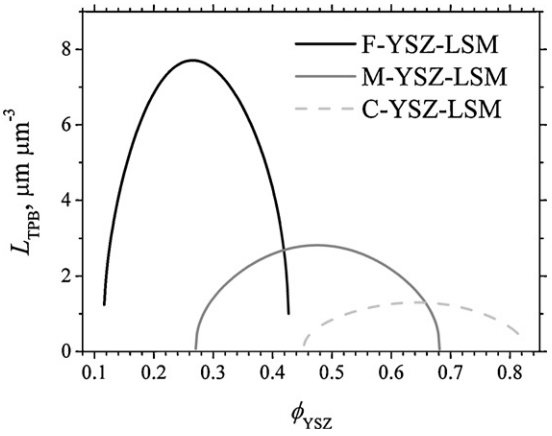

Fig. 8. Active TPB length for F-YSZ–LSM, M-YSZ–LSM and C-YSZ–LSM electrodes as a function of YSZ loading ($\phi_g = 0.3$) calculated with particle size from the source powders.

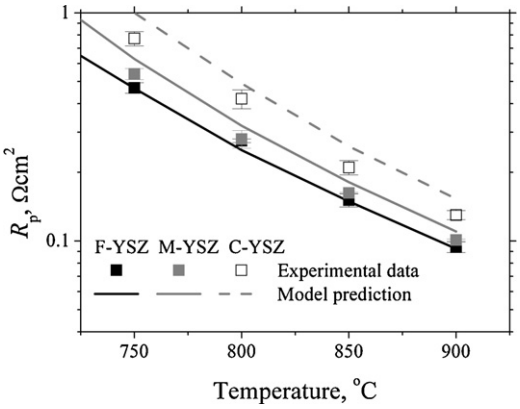

Fig. 9. Interfacial polarization resistances of F-YSZ–LSM, M-YSZ–LSM and C-YSZ–LSM electrodes as a function of temperature ($\phi_g = 0.3$, $\delta = 50\,\mu m$). Data is estimated with size parameters of the source powders.

Fig. 9 shows the comparison in interfacial polarization resistances as estimated from the powder size and determined with impedance spectroscopy for F-YSZ–LSM, M-YSZ–LSM, and C-YSZ–LSM electrodes. YSZ volume fraction is 0.26, 0.48 and 0.64 for F-YSZ–LSM, M-YSZ–LSM, and C-YSZ–LSM electrodes, respectively. The composition is set according to the maximum TPB length (Fig. 8). The resistivity is a function of temperature, which is derived from Ref. [9]. As shown in Fig. 9, the experimental results generally agree with the estimation, especially for the electrode based on fine YSZ. For example, the experimental resistance of F-YSZ–LSM electrode is 0.26 Ω cm^2 at 800 °C, while the estimated resistance is 0.25 Ω cm^2. For F-YSZ–LSM electrode, the average difference between the experimental and estimated results is only 3%. However, the difference is big for the electrode prepared with the coarse YSZ, −18%. But the prediction is also not too bad. Estimation with source particles is limited by the sintering process, in which sintering temperature, time, and even heating rate affect the size and shape of the particles in the resulted electrodes. Such estimation will become much more reliable and can reveal the real electrode performance if the sintering process is clear, especially the process for electro-catalyst, which is much easier to be sintered than the electrolyte.

5. Conclusion

An analytical model is proposed to estimate the effects of particle size and its distribution on the electrochemical performance and microstructure features of SOFC electrodes. Active TPB length per unit volume and interfacial polarization resistance are calculated and the results are in accordance with literature and experimental data. The model produces explicit insight and quantitative design guidance for electrode fabrication, and leads to the following conclusions:

(1) The effects of particle size distribution are sensitive to its sampling object. When the sampling object is particle volume/number, the particles with a wide size distribution lead to a higher/lower maximum TPB length as compared to its mono-size particles. The difference is more significant for a wider distribution.
(2) Distribution with the sampling object as volume/number can shift the optimal composition corresponding to the maximum active TPB length. When *j* type particles have a wider distribution compared with *i* type particles, less/more *j* phase loading is required compared with its mono-size case.
(3) It is possible to estimate electrode performance with the particle size and distribution of source materials. Consequently, SOFC performance can be theoretically predicted with size parameters of the starting oxide powders, suggesting a from-powder-to-power approach.

Acknowledgements

We thank gratefully acknowledge the Natural Science Foundation of China (10979046 and 50730002) and the U.S. National Science Foundation (CBET 0967166).

References

[1] Z.P. Shao, S.M. Haile, Nature 431 (2004) 170–173.
[2] X.J. Chen, S.H. Chan, K.A. Khor, Electrochim. Acta 49 (2004) 1851–1861.
[3] S.B. Adler, Chem. Rev. 104 (2004) 4791–4843.
[4] D.H. Jeon, J.H. Nam, C.J. Kim, J. Power Sources 139 (2005) 21–29.
[5] H. Fukunaga, M. Ihara, K. Sakaki, K. Yamada, Solid State Ionics 86–88 (1996) 1179–1185.
[6] B. Kenney, M. Valdmanis, C. Baker, J.G. Pharoah, K. Karan, J. Power Sources 189 (2009) 1051–1059.
[7] W. Zhu, D. Ding, C. Xia, Electrochem. Solid-State Lett. 11 (2008) B83–B86.
[8] P. Costamagna, P. Costa, V. Antonucci, Electrochim. Acta 43 (1998) 375–394.
[9] Y.X. Zhang, C.R. Xia, J. Power Sources 195 (2010) 4206–4212.
[10] A.M. Gokhale, S. Zhang, M. Liu, J. Power Sources 194 (2009) 303–312.
[11] J.R. Wilson, W. Kobsiriphat, R. Mendoza, H.Y. Chen, J.M. Hiller, D.J. Miller, K. Thornton, P.W. Voorhees, S.B. Adler, S.A. Barnett, Nat. Mater. 5 (2006) 541–544.
[12] J.R. Wilson, J.S. Cronin, A.T. Duong, S. Rukes, H.-Y. Chen, K. Thornton, D.R. Mumm, S. Barnett, J. Power Sources 195 (2010) 1829–1840.
[13] L.A.L. Tarte, J.R. Cournoyer, K. Dovidenko, E.J. Olson, J.A. Ruud, T. Striker, Microsc. Microanal. 11 (2005) 846–847.
[14] S. Zhang, M. Lynch, A.M. Gokhale, M. Liu, J. Power Sources 192 (2009) 367–371.
[15] J.H. Choi, J.H. Jang, S.M. Oh, Electrochim. Acta 46 (2001) 867–874.
[16] D.F. Chen, Z.J. Lin, H.Y. Zhu, R.J. Kee, J. Power Sources 191 (2009) 240–252.
[17] C. Zhang, W.Y. Li, M.P. Planche, C.X. Li, H.L. Liao, C.J. Li, C. Coddet, Surf. Coat. Technol. 202 (2008) 5055–5061.
[18] H.J. Cho, G.M. Choi, J. Power Sources 176 (2008) 96–101.
[19] C. Monterrubio-Badillo, H. Ageorges, T. Chartier, J.F. Coudert, P. Fauchais, Surf. Coat. Technol. 200 (2006) 3743–3756.
[20] J.R. Wilson, A.T. Duong, M. Gameiro, H.Y. Chen, K. Thornton, D.R. Mumm, S.A. Barnett, Electrochem. Commun. 11 (2009) 1052–1056.
[21] X.M. Wang, C.X. Li, C.J. Li, G.J. Yang, Int. J. Hydrogen Energy 35 (2010) 3152–3158.
[22] M.I. Mendelson, J. Am. Ceram. Soc. 52 (1969) 443–446.
[23] D. Chen, W. Bi, W. Kong, Z. Lin, J. Power Sources 195 (2010) 6598–6610.